Magnetically recoverable *Ni@C* composites: the synthesis by carbonization and adsorption for Fe^{3+}

Xiaowen Wu[a,*], Zhijie Zhang[a], Chao Xia[a], Biqiong Chen[b], Xiaozhao Jin[a], Zhaohui Huang[a], Yan-gai Liu[a], Minghao Fang[a], Xin Min[a]

[a] *Beijing Key Laboratory of Materials Utilization of Nonmetallic Minerals and Solid Wastes, National Laboratory of Mineral Materials, School of Materials Science and Technology, China University of Geosciences, Beijing 100083, P.R. China*

[b] *Department of Materials Science and Engineering, University of Sheffield, Mappin Street, Sheffield, S1 3JD, United Kingdom*

Abstract

Carbon-encapsulated nickel particles (*Ni@C* composites) for removing Fe^{3+} in wastewater have been prepared by the carbonization of phenolic resin mixing with nickel particles. XRD results reveal that the *Ni@C* composites are consisted of C, Ni, and Ni$_3$S$_2$. The TG-DTG curves of *Ni@C* composites are almost same as that of phenolic resin. The morphology investigation shows that Ni is distributed randomly on carbon. Based on analysis of N$_2$ adsorption-desorption isotherm, the surface area and pore volume of *Ni@C* composites are 187.47 m$^2\cdot$g^{-1} and 0.06900 cm$^3\cdot$g$^{-1}\cdot$nm^{-1}, respectively. The saturation magnetization values for *Ni@C* composites are 68.99 emu$\cdot$g^{-1} determined by the Vibrating Sample Magnetometer. *Ni@C* composites

*Corresponding author. Dr Xiaowen Wu. Correspondence address: School of Materials Science and Technology, China University of Geosciences (Beijing), 29 Xueyuan Road, Beijing, 100083, China. Tel. & Fax: +86 (10) 8232 2039. E-mail address: xwwu@cugb.edu.cn

exhibit a high adsorption capacity for Fe^{3+}. The adsorption behavior follows the

pseudo-second-order kinetic and Langmuir model between the adsorbents and Fe^{3+}.

Furthermore, the adsorption capacity of *Ni@C* composites derives from the attractive

force between the adsorbed anion and the surface positive charge of *Ni@C*

composites, as well as the bond between the adsorbed cation and the COO^- groups.

From the above results *Ni@C* composites can be widely applied in wastewater

treatment as a new efficiency and excellent recoverable adsorbent.

1. Introduction

Iron and its compounds are contaminants and commonly found in wastewater

produced by several industries, including plating, minerals, and cements [1]. Fe^{3+} is

toxic and can pose risks to human health such as gastrointestinal disease [2]. It is

dreadful even of people just take in a low amount of Fe^{3+} at 60 $mg \cdot kg^{-1}$ of body

weight [3].

In the past few decades, some processes of removing Fe^{3+} in wastewater, such as

flocculation [4], bacterial action [5], reverse osmosis [6], and adsorption [7]. Among

them, adsorption is more prone to wider applications in industrial treatment because

of its low initial cost and flexibility in design and operation [8]. In particular,

carbonaceous materials, such as porous carbon [9], active carbon [10], carbon

nanotubes [11], and carbon fibers [12], are common adsorbent materials because of their high specific surface area and good sorption capacity for pollutant [13], and wide availability of precursors [14-19]. Phenolic resin (PR) was usually selected as carbon source because it gives high production yield on account of its ability to polymerize and form complex carbon molecules [20].

Recently, magnetic separation technologies have been attracting more and more attention [21-22]. With the assistance of magnetic force, magnetic matter can be separated from the solution efficiently regardless of its size. Nickel (Ni) has been widely used as a magnetic material because of their excellent magnetic properties. Thus, magnetic *Ni@C* particles are regarded as a promising sorbent for removing heavy metals because of the strong adsorption capacity for metal ion and good magnetic separation performance. Xiao et al. [23] reported that the *Ni@C* composites can be used as adsorbent for heavy metal ions. It has been widely reported *Ni@C* nanocomposites are composed of nickel nanoparticles coated within a layer of thin carbon shell [24-26]. However, small nanoparticles aggregate together easily due to high surface energy [27].

Herein, we proposed to use *Ni@C* composites as sorbent instead of *Ni@C* nanocomposites to resolve the problem of agglomeration. *Ni@C* composites were synthesized by carbonization with nickel powder and PR as the raw materials in the present work. Carbon materials from the pyrolysis of PR are porous and have good

3

adsorption capacity [28-29]. The size of Ni particles is micron-scale rather than nano-scale, so the Ni powder avoids the agglomeration of nanoparticle. Importantly, the metal powder of Ni has stronger magnetism than Ni nanoparticle synthesized from organic compounds. Thus, the magnetism of *Ni@C* composites can be stronger than that of *Ni@C* naonocomposites, attributing to separate sorbents from solution more easily. Besides, the preparation process of *Ni@C* composites is easier than that of *Ni@C* naonocomposites, and the material cost of *Ni@C* composites is cheaper than that of *Ni@C* naonocomposites.

In this study, the microstructure and properties of *Ni@C* composites, such as phase, morphology, specific surface area, pore size, magnetic properties and adsorption capacity for Fe^{3+}, were investigated in details. Moreover, the adsorption kinetics and isotherm for Fe^{3+} from water solution onto *Ni@C* composites, and the adsorption mechanism of Fe^{3+} on *Ni@C* composites were analyzed intensively.

2. Experimental

2.1 *Chemicals*

Nickel powder (200 mesh, purity of 99.9%), silane coupling agent, and p-toluenesulfonic acid were purchased from Beijing Chemical Works. *PR*, HCl, NaOH, was provided by Jingtong Leitai Chemical Product Co. Ltd. in China. All reagents were used as-received, without further treatment.

2.2 *Synthesis of Ni@C composites*

In a typical synthesis as shown in **Figure 1**, the raw materials of *PR* (10 gram), nickel powder (2.31 gram), and silane coupling agent (0.77 gram) were successively added and then mixed by stirring in a beaker. After stirring for 10 min, p-toluenesufonic acid (2.31 gram) was added to the mixture and mixed for 10 min, and the mixture cured naturally for 15 min at room temperature. Then, the composite precursor was put in the furnace (GL-1100M, Siyang Jingmi Shebei Co. Ltd), and the carbonization process took place in the condition of non-oxygen. The samples were heated from room temperature to 850 $^{\circ}$C at a heat rate of 2 $^{\circ}$C·min^{-1} and maintained for 2 hours at 850 $^{\circ}$C. Finally, the samples were cooled down naturally, and *Ni@C* composites were obtained.
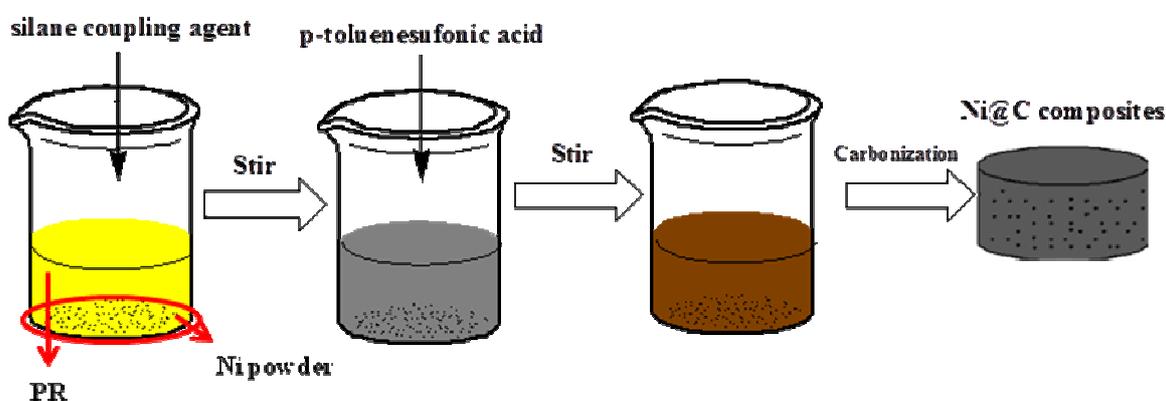
Fig.1 Schematic illustration of the synthesis of *Ni@C* composites

2.3 *Characterization*

The phases of *Ni@C* composites were detected by X-ray diffraction (XRD, Rigaku D/max-RB, Japan) at 40 kV and 120 mA with Cu Kα radiation. The

differential thermal analysis and thermogravimetric analysis (TG) were tested on the thermogravimetric analyzer (NETZSCH STA 409 C/CD, Germany) in argon atmosphere. The morphologies and microstructures of *Ni@C* composites were observed by scanning electron microscopy (SEM, JEOL JSM-840A, Japan) at the voltage of 15 kV. Brunauer-Emmett-Teller (BET) surface areas and the pore size distribution of *Ni@C* composites were determined by the Autosorb IQ2 analyzer (Quantachrome Model 2000, USA). The magnetic properties of specimen were investigated by the superconducting quantum interface device (SQUID) magnetometer (Quantum Design PPMS-9). FTIR (Infinity Gold, Thermo Mattson, USA) was used to analyze the difference in surface functional groups of *Ni@C* composites before and after adsorption. Zeta potential of the specimens in various pH value solutions were detected by mütek SZP-04.

2.4 *UV-Vis measurement*

The adsorption experiments for Fe^{3+} on *Ni@C* composites were carried out by using the water solution of $FeCl_3$ to evaluate the parameters of adsorption. The centrifuge tube containing the solid sample and the solution was shaken at the speed of 160 rpm in the horizontal shaker (HY-5A, Jintan Tianjing Laboratory Instrument) at room temperature for different periods of time as follows: 1, 5, 10, 30, 60, 120 and 180 min. The mass of *Ni@C* composites, the concentration and volume of Fe^{3+} solution used in each experiment were 0.1 g, 3000 mg·L^{-1}, and 25 mL, respectively.

The adsorption isotherm for Fe^{3+} on *Ni@C* composites was performed by mixing *Ni@C* composites with Fe^{3+} solution at various initial concentrations of 100, 200, 500, 800, 1200, 2000, 3000, 5000, 6000 and 10000 $mg \cdot L^{-1}$, as well the same parameters of shaking speed (160 rpm) and time (2 h) in the centrifuge tubes on the horizontal shaker.

To investigate the effect of pH value of solution on the adsorption capacity, a changed initial pH value of the mixing solution was used by adjusting the concentration of HCl (1 $mol \cdot L^{-1}$ and 0.1 $mol \cdot L^{-1}$) or NaOH (0.01 $mol \cdot L^{-1}$ and 0.001 $mol \cdot L^{-1}$) solution while the concentration of Fe^{3+} solution was fixed at 5000 $mg \cdot L^{-1}$. The pH value of solution was measured every 4 hours and re-adjusted until the pH value stabilized at the desired final values of 1, 2, 3, and 10. The total mixing time was 12 h.

After a desired period of time, all mixtures were centrifuged for 15 min at 8000 rpm, and the supernatants were filtered through 0.45 μm syringe filters for remaining Fe^{3+} solution after adsorption. The amount of Fe^{3+} adsorbed was determined by the UV-Vis spectroscopy (759S, Shanghai Jingke Co., Ltd) and calculated by the following equation (1) [30].

$$q_e = V(C_i - C_e)/W \tag{1}$$

Where V is the volume of Fe^{3+} solution in millilitre, C_i and C_e are the initial and final concentrations ($mg \cdot L^{-1}$) of Fe^{3+} in solution, respectively, and W is the weight (g) of $Ni@C$ composites.

3. Results and discussion

3.1 *Microstructure of the synthetic Ni@C composites*

Figure 2 shows the XRD patterns of $Ni@C$ composites, Ni powder, and *PR* after carbonization. There are obviously sharp diffraction peaks at 2θ of 44.56^o and 51.92^o, attributable to (111) and (200) peaks of nickel [23]. Besides, heazlewoodite (Ni_3S_2) derived from the reaction between Ni powder and S from the pyrolysis of p-toluenesulfonic. Furthermore, the curve bread is observed in the XRD pattern of *PR*, which indicated that the carbon produced from the pyrolysis of *PR* was amorphous.
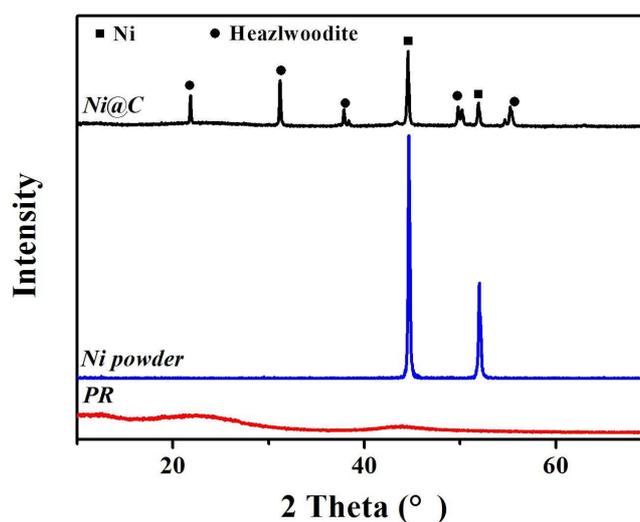
Figure 2. The XRD pattern of *Ni@C* composites, Ni powder, and PR after carbonization.

As shown in **Figure 3**, it can be seen that the pyrolysis process of *PR*, Ni powder, and the mixture of Ni and *PR* (*Ni@PR*) in argon atmosphere. The pyrolysis of *Ni@PR* comes from the pyrolysis of *PR* rather than Ni powder, due to the excellent phase stability of Ni powder in argon atmosphere at the temperature less than 1000 $^{\circ}$C. The pyrolysis of *Ni@PR* could be divided into four stages at 0~1000 $^{\circ}$C as follows [31]. Stage 1 at the temperature less than 230 $^{\circ}$C is attributed to the dehydration on the *Ni@PR*. In comparison with the DTG curve of *PR*, there is an obviously endothermic valley on the DTG curve of *Ni@PR* in stage 2, which indicated that producing Ni_3S_2 could be occurred in stage 2 with the pyrolysis of p-toluenesulfonic. The degradation in forms of CO or CO_2 molecules from organic chemical occurs in stage 3 at the range of 450~750 $^{\circ}$C. The moderate mass loss step for stage 4 begun at around 750 $^{\circ}$C is associated with the consideration of carbons and removal of hetero atoms from solid phase.
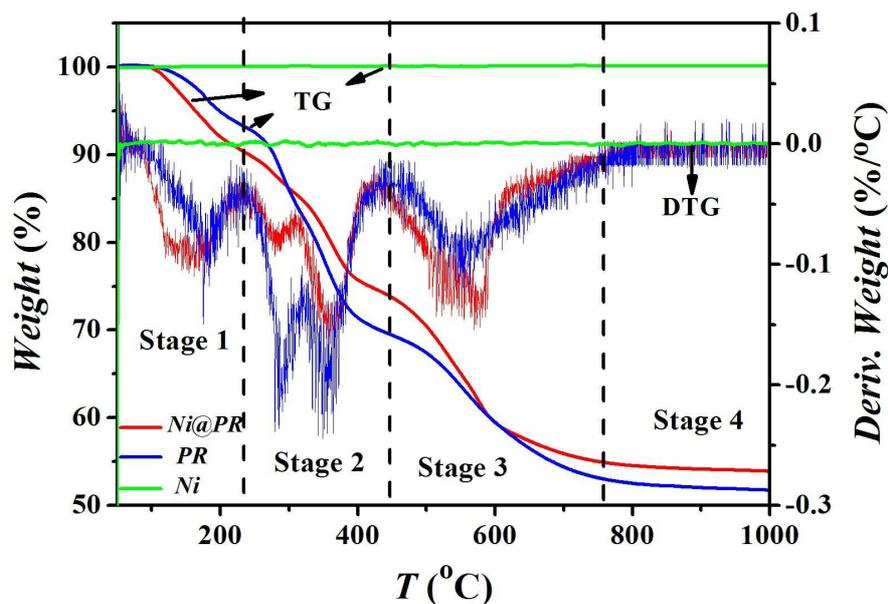
Figure 3. The TG-DTG curves of *Ni@PR*, *PR*, and Ni powder.

Figure 4 shows the typical SEM micrographs of *Ni@C* composites. The size of particles is microscale rather than nanoscale (**Figure 4a**). On the basis of the result of the energy dispersion spectrometer (EDS) (**Figure 4b**) and the EDX area scanning (**Figure 4c**), the principal component of *Ni@C* composites is carbon. Moreover, Ni is distributed randomly over carbon (**Figure 4d**). Importantly, large pores are not observed on the surface of *Ni@C* composites, which is coincident with the pore size distribution plotted in **Figure 5b**. The pore diameter of *Ni@C* composites is about 0.5575 nm close to 1.5 times as wide as the molecular diameter of carbon oxides (CO or CO_2), H_2O, and olefin with low carbon, which is difficult to be observed by SEM. Meanwhile, it could be inferred that the pores of *Ni@C* composites were derived from the pyrolysis of *PR* which produced gas at the molecular scale. **Figure 5a** is the BET image of *Ni@C* composites, and displays a high surface area of 187.47 $m^2 \cdot g^{-1}$ which is

beneficial to provide more active sites [32]. This is the reason why $Ni@C$ composites have the higher adsorption capacity.
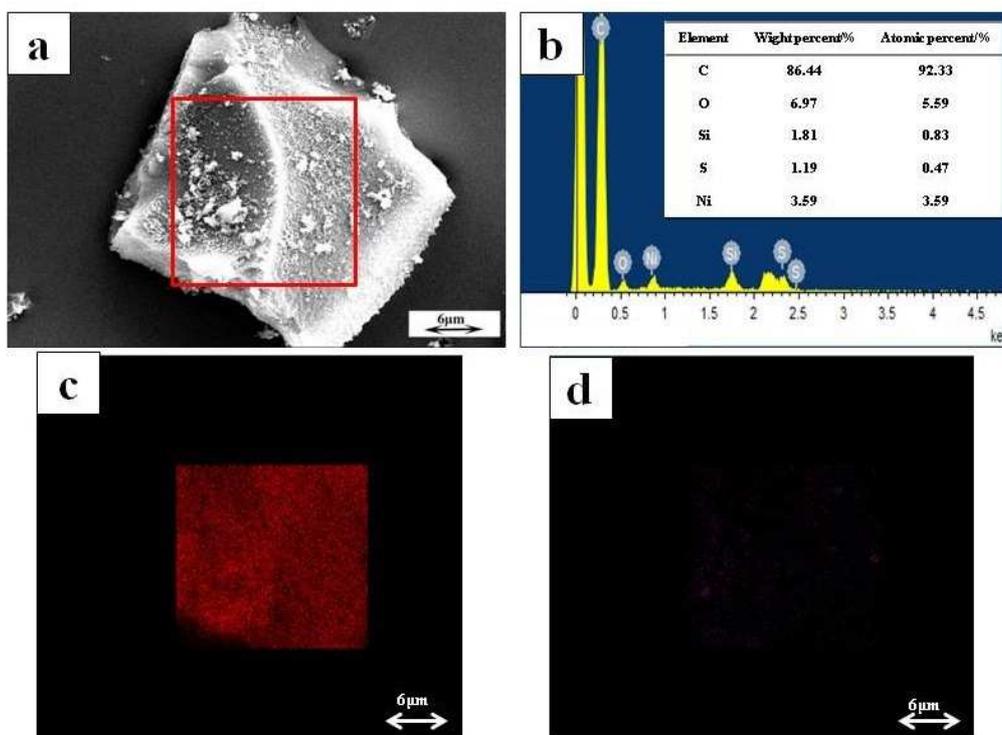
Figure 4. Typical SEM micrograph (a), the EDS of red inside rectangle (b),

EDX area-scan of elements C (c), and Ni (d) of $Ni@C$ composites
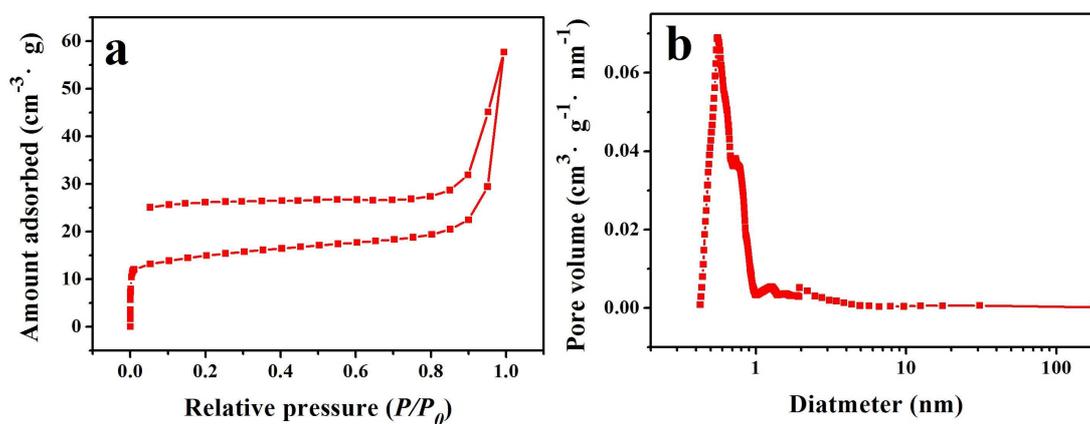
Figure 5. (a) N_2-adsorption-desorption isotherms and (b) corresponding pore

size distribution curves of the $Ni@C$ composites

Figure 6 displays the ferromagnetic properties of *Ni@C* composites. It can be seen that the *Ni@C* composites are attracted firmly to the magnet so that the powder could not fall to the bottom of bottle, which endows them to be magnetically separable adsorbents for heavy metal ions. Besides, the value of saturation magnetization (M_s), remnant magnetization (M_r) and coercivity (H_c) can be calculated from the magnetization curves, and the results are listed as follow: M_s, 68.99 emu·g^{-1}; M_r, 4.07 emu·g^{-1}; H_c, 4.3 Oe. In contrast with synthetic *Ni@C* nanocomposites where the source of Ni was from inorganic salt or metal organic compounds [23, 27, 33], the values of *Ms* and *Mr* are greater, and the value of *Hc* is lower, which demonstrated the feature made it easiest to spread and separate among the cycles of adsorption [34, 35].
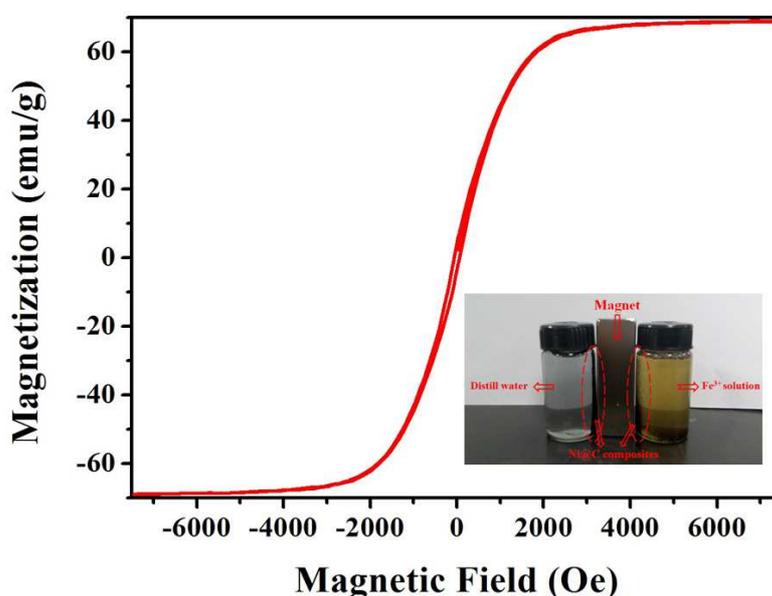
Figure 6. Room-temperature M-H hysteresis curve of *Ni@C* composites.

Inset: photograph (lower right) of the magnetic properties of *Ni@C* composites

near the magnet.

3.2 *The standard curve of concentration of Fe^{3+} ions*

Six groups of Fe^{3+} solution with the concentrations of 20, 40, 60, 80, 100, and 120 mg·L^{-1} respectively were prepared. They were measured with the addition of sulfosalicylic acid in visible light with the wavelength of 466 nm [36]. Absorbance value was converted into concentration data, and then the standard curve of Fe^{3+} concentration was determined, shown in **Figure 7**.

According to the Lambert-beer's law [37], $A=Kbc$, where A is absorbance; K is proportional constant; b is the thickness of standard quartz cell for spectrophotometry (cm); c is the concentration of solution in the standard quartz cell for spectrophotometry (mg·L^{-1}). Absorbance is proportional to the Fe^{3+} concentration of solution in the standard quartz cell for spectrophotometry. The linear equation (y=0.0165x+0.0385, R^2=0.9985) obtains from the experiments which accords the Lambert-beer's law well. Therefore, spectrometric method could be used to accurately measure the concentration of Fe^{3+} in the standard quartz cell for spectrophotometry.
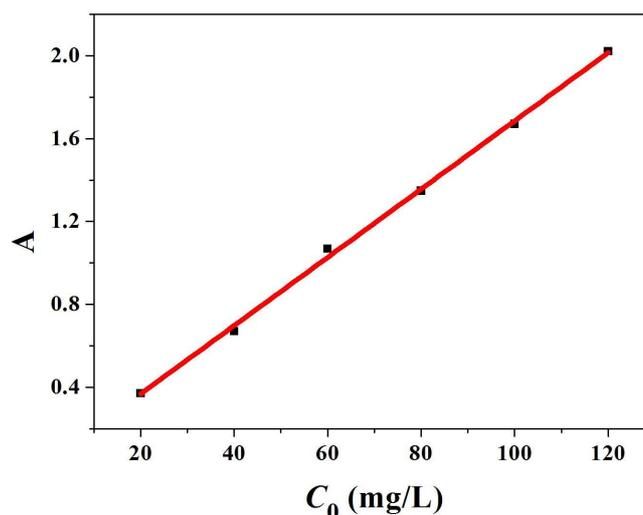
Figure 7. The standard curve of Fe^{3+} concentration in solution.

3.3 *The adsorption kinetics of Fe^{3+} ions on Ni@C composites*

Figure 8 shows the influence of adsorption time on the adsorption quantity and two fitting curves of adsorption reaction kinetics. It can be seen that the initial adsorption rate for Fe^{3+} is faster. When the adsorption time go to 60 min, the adsorption quantity for Fe^{3+} on *Ni@C* composites increases significantly to 691 mg·g^{-1}. After 60 min, the adsorption rate for Fe^{3+} begins to slow down relatively in a trend, and adsorption quantity achieves plateau and equilibrium.

The final adsorption quantity is 740.35 mg/g and the removal rate is over 98.71% which is better than the removal rate of activated carbon, 70.51% [38, 39]. It was reported that the adsorption degree for some toxic elements on activated carbon extends from high to as low as none (e.g. Sb^{3+}, As^{3+}, Bi^{3+} high; Co^{2+}, Hg^{2+}, Ag^+ good; Fe^{3+}, Pb^{2+}, Ni^{2+}, complexed Cu^{2+} fair; Cd^{2+}, Cu^{2+}, Zn^{2+}, Mn^{2+}, Fe^{2+}, Ba^{2+} low to none) [36]. The removal rate of Pb^{2+} on *Ni@C* nanocomposite has been

14

reported to be 92% [31], close to the removal rate of Fe^{3+} on $Ni@C$ composites reported here.

The adsorption reaction kinetics is constructed with pseudo first order kinetic equation and pseudo second order kinetic equation according to the following equations (2) and (3) [40, 41].

$$q_t=(1-e^{-k_1 t})q_1 \qquad\qquad\qquad (2)$$

$$t/q_t=1/(k_2\times q_2)^2+t/q_2 \qquad\qquad\qquad (3)$$

where q_t (mg·g^{-1}) is the adsorption quantity at t min; k_1 (mg·g^{-1}·min^{-1}) and k_2 (mg·g^{-1}·min^{-1}) are the first-order and second-order kinetics rate constants respectively; q_1 (mg·L^{-1}) is the equilibrium adsorption quantity of first-order kinetic adsorption model; q_2 (mg·L^{-1}) stands for the equilibrium adsorption quantity of second-order kinetic adsorption model.

The results of two parameters, kinetics rate constant and equilibrium adsorption quantity, from the fitting linear equations are compiled in Table 1. It can be seen from the data comparison that the fitting curve of pseudo second-order kinetics equation is better than that of pseudo first-order equation. Also, the maximum theoretical adsorption quantity of pseudo second-order kinetic equation is 769.23 mg·g^{-1}, which is closer to the maximum experimental adsorption quantity, 740.35 mg·g^{-1}, than that of the pseudo first-order kinetic equation, 681.73 mg·g^{-1}. The squared correlation coefficient of fitting linear of

pseudo second-order kinetics equation is 0.9989 which is higher than that of pseudo first-order kinetics equation, 0.9438, and the higher correlation coefficients ($R^2 > 0.99$) indicate that the adsorption followed the pseudo second-order kinetics mechanism, and the adsorption process is controlled by a chemical process involving forces through sharing or exchange of electrons [42].
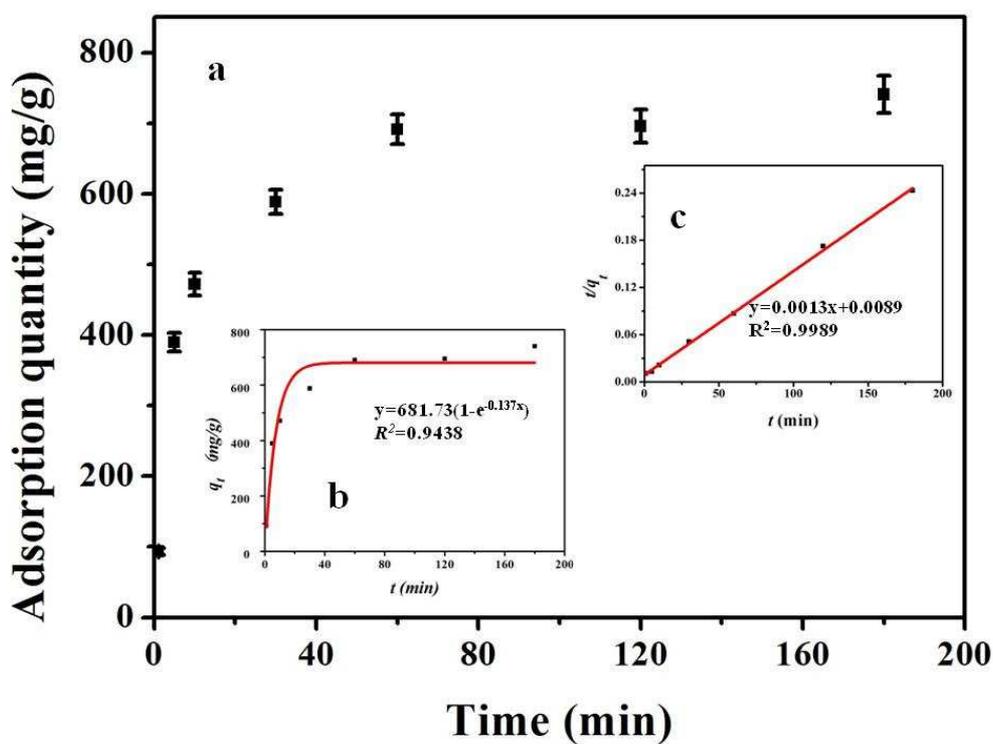
Figure 8. Kinetics of adsorption on *Ni@C* composites (a); the solid lines show the theoretical values from the pseudo-first-order (b), and pseudo-second-order (c) respectively. Data plots represent the experimental data.

Table 1. The adsorption kinetic parameters for Fe^{3+}.

Pseudo first order kinetic equation			Pseudo second order kinetic equation		
k_1 (mg·g^{-1}·min^{-1})	q_1 (mg·g^{-1})	R^2	k_2 (mg·g^{-1}·min^{-1})	q_2 (mg·g^{-1})	R^2
1.37×10^{-1}	681.73	0.9438	1.38×10^{-2}	769.23	0.9989

3.4 *Adsorption isotherm*

The phenomenon of Fe^{3+} adsorption on *Ni@C* composites is described by an adsorption isotherm with respect to the mobility of Fe^{3+} from water to *Ni@C* composites at equilibrium in a constant pH value and temperature.

Two well-known adsorption isotherm models, namely, the Langmuir model and Freundich model, are widely employed to analyze the adsorption isotherm date. The linear forms of the above two models are presented in equations (4) and (5) [43].

Langmuir: $C_e/q_e = C_e/q_m + 1/q_m k_L$ (4)

Freundlich: $\ln q_e = \ln C_e/n_F + \ln k_F$ (5)

Where C_e is the concentration of Fe^{3+} at equilibrium (mg·L^{-1}), q_e is the amount of Fe^{3+} adsorbed per gram of *Ni@C* composites (mg·g^{-1}), q_m is the maximum adsorption quantity in theory, n_F is a heterogeneity factor. Besides, k_L and k_F are constants related to Langmuir and Freundlich, respectively.

Compared to Freundlich isotherms, Langmuir model is better to describe the Fe^{3+} adsorption process with the higher determination coefficient $R^2=0.9955$, as shown in **Figure 9**. The good fitting with Langmuir describes that adsorption takes place at specific homogenous sites within the adsorbent, and each site binds to only a single adsorbate [44]. On the basis of the slope and intercept values of the fitting straight-line, it could be inferred that $q_m=1250$ mg·g^{-1}, which close to experimental data 1145 mg·g^{-1}.
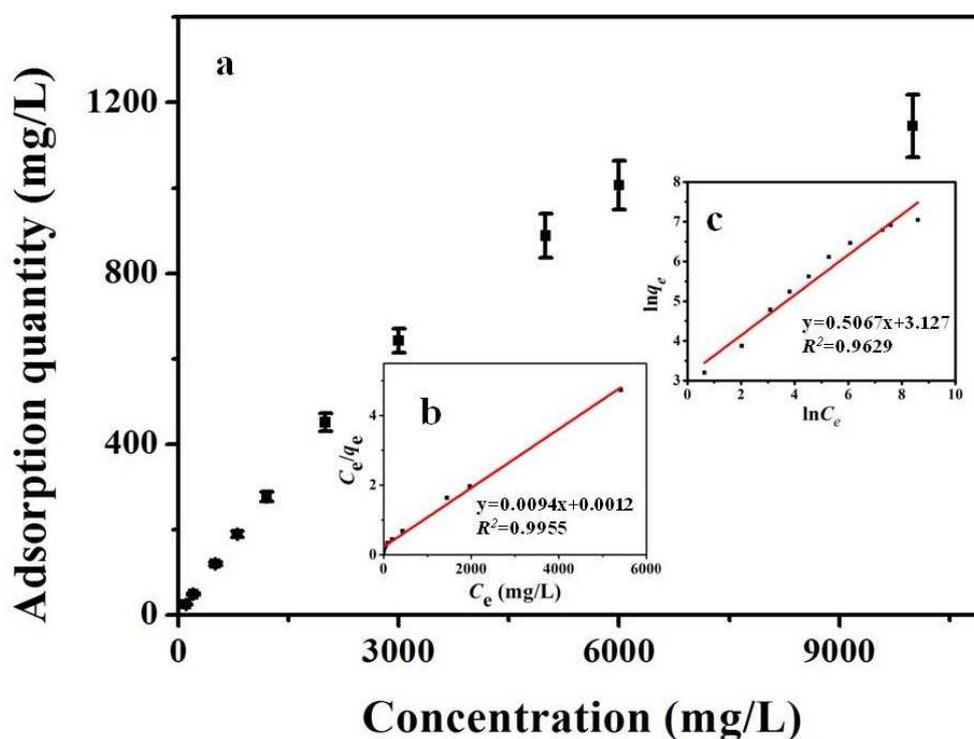
Figure 9. The adsorption curve of Fe^{3+} ions on *Ni@C* composites (a); the solid lines show the theoretical values from the Langmuir (b), and the Freundlich (c) respectively. Data plots represent the experimental data.

3.5 *The effect of pH value on adsorption for Fe^{3+}*

Figure 10 displays the influence of pH value on adsorption capacity of *Ni@C* composites for Fe^{3+}. In the conditions of strong acid, the adsorption capacity of *Ni@C* composites for Fe^{3+} is the best in solutions with various pH values. Furthermore, the adsorption quantity of *Ni@C* composites for Fe^{3+} in the condition of pH value=1 is higher than that in the circumstance of pH value =2. The reason could be explained by the fact that the positive surface charge decreased with acid in solution gradually. On the basis of the zeta potential of specimens in solutions with pH value=1 and pH value=2, the zeta potential of the former is greater than that of the latter in accordance with the above explanation. Thus, the positive surface charge may play an important role in adsorption mechanism of *Ni@C* composites.

However, the calculated adsorption quantity elevates suddenly in the conditions of pH value over 3, which could be derived from the hydrolysis of Fe^{3+} as shown in the two lower graphs. When pH value is at 3 and 10, there is rufous precipitation in Fe^{3+} solution. Thus, it is not necessary to study and discuss the adsorption capacity of *Ni@C* composites when pH value is over 3.
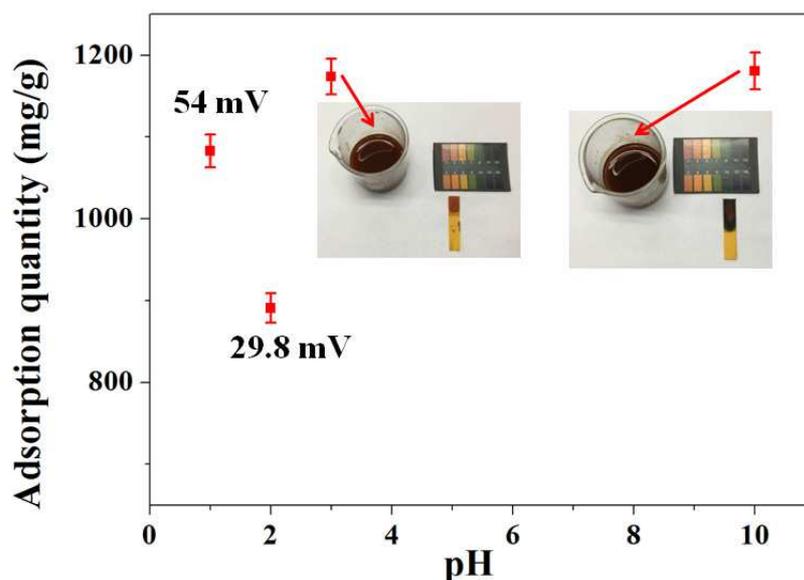
Figure 10. The influence of pH value on the adsorption quantity of *Ni@C* composites for Fe^{3+}.

3.6 *The analysis of functional groups on Ni@C composites*

The surface functional groups of *Ni@C* composites, $FeCl_3$ and Fe^{3+}-adsorbed *Ni@C* composites in the conditions of various pH values were analyzed by the FTIR spectroscopy and the results are shown in **Figure 11**. There are no obvious infrared characteristic peaks in the FTIR spectra of *Ni@C* composites, which could be caused that the structure of *Ni@C* composites was symmetrical and so there was rarely asymmetric stretch. At 3369 and 3390 cm^{-1}, there are strong peaks, attributed to –OH and H_2O resulted from crystallized water of $FeCl_3$ and adsorbed water on *Ni@C* composites, respectively [45].

The peaks at 1585 and 459 cm^{-1} could be assigned to the stretching vibration of Fe-Cl group. After adsorbing Fe^{3+}, the peak at around 460 cm^{-1} remains at the

20

FTIR spectra of Fe^{3+}-adsorbed *Ni@C* composites, indicating some Fe-Cl groups could be attracted by attractive force from the charges on the surface of *Ni@C* composites. As shown in the previous section (the effect of pH value on adsorption), there are the positive surface charges when pH values are 1 and 2. Thus, it was inferred that the Fe-Cl groups could be anionic. The attractive force between Fe-Cl anionic groups and surface charge elevated with increasing quantity of positive surface charge so that the adsorption quantity decreased with less acid in the solution.

Nevertheless, the peak at 1585 cm^{-1} vanishs, while the skeleton vibration peaks of -COO groups at around 1620 and 1400 cm^{-1} appears [46], suggesting that some COOH groups could reacted with Fe-Cl groups. Therefore, the Fe-Cl groups were cationic, which could replace H^+ site to combine with COO^- to form a covalent bond.

Overall, the anionic and cationic Fe-Cl groups were primary adsorbents. As a consequence, it was assumed that $FeCl_3$ existed in the forms of $[FeCl_4]^-$ and $[FeCl_2]^+$ in water. $[FeCl_4]^-$ was attracted by the positive surface charge and $[FeCl_2]^+$ replaced H^+ site to combine with COO^-.
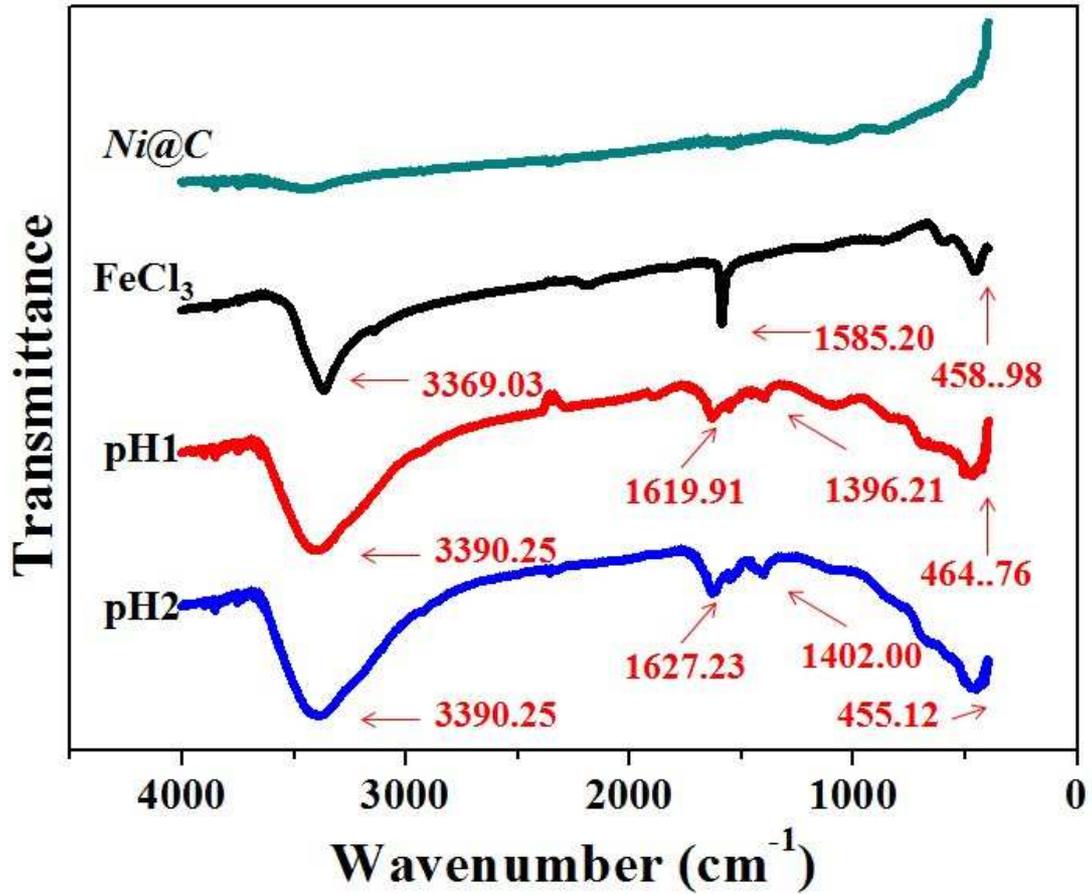
Figure 11. FTIR spectra of *Ni@C* composites, FeCl$_3$ and Fe^{3+}-adsorbed

Ni@C composites in different pH value conditions.

4. Conclusions

In summary, magnetically recoverable *Ni@C* composites with larger surface

areas were synthesized by a simple and effective carbonization method. The

Ni@C composites have not only strong magnetism, but also large specific

surface area (determined to be 187.47 m$^2\cdot$g^{-1}), so it can be used as potential and

intriguing adsorbents to remove heavy metal ion from wastewater. The

adsorption processes were investigated by the kinetics and adsorption isotherms.

The results show that the adsorption for Fe^{3+} on the *Ni@C* composites followed

the pseudo second-order kinetics and better fitted to the Langmuir model than the Freundlich model. Besides, the adsorption capacity of *Ni@C* composites derived from attractive force between adsorbed anion and the surface positive charge of *Ni@C* composites, and the chemical bond between adsorbed cation and COO^- groups. Because of the excellent performance showed above, the *Ni@C* composites can contribute to environmental protection.`

Acknowledgements

References

[1] Y.F. Cao. The modification of diatomite and its application in the treatment of ferri wastewater. China, Central South University of Forestry and Technology, 2010.

[2] J.M. Sieliechi, G. Kayem, I. Sandu. Effect of water treatment residuals (aluminum and iron ions) on hunman health and drinking water distribution system. Int. J. Conserv. Sci, 1 (2010): 175-182.

[3] M. El-Harbawi, A. Sabidi, E. Kamarudin, et al. Design of a portable dual purpose water filter system. J. Eng. Sci. Technol. 5 (2010): 165-175.

[4] Z.K. Xiong, J.Y. Cao, D. Yang, et al. Coagulation-flocculation as pre-treatment

for micro-scale Fe/Cu/O_3 process (CF-mFe/Cu/O_3) treatment of the coating wastewater from automobile manufacturing. Chemosphere, 166(2017): 345-341.

[5] C. Delaire, C. M. van Genuchten, S.E. Amrose, et al. Bacteria attenuation by electrocoagulation governed by interactions between bacterial phosphate groups and Fe (Ⅲ) precipitates. Water Research, 103 (2016): 74-82.

[6] H.J. Sung, T. Berrin. Novel technologies for reverse osmosis concentrate treatment: A review. Journal of Enviromental Management, 150 (2015): 322-335.

[7] Ensar Oguz. Fixed-bed column studies on the removal of Fe^{3+} and neural network modeling. Arabian Journal of Chemistry, 10 (2017): 313-320.

[8] U. Habiba, A.M. Afifi, A. Salleh, et al. Chitosan/ (polyvinyl alcohol)/ zeolite electrospun composite nanofibrous membrane for adsorption of Cr^{6+}, Fe^{3+} and Ni^{2+}. Journal of Hazardous Materials, 322 (2017): 182-194.

[9] A.T Xie, J.D Dai, X. Chen, et al. Ultrahigh adsorption of typical antibiotics onto novel hierarchical porous carbon derived from renewable lignin via halloysite nanotubes-template and in-situ activation.. Chemical Engineering Journal, 304 (2016): 609-620.

[10] Y.H. Cao, Y. Gu, K.L Wang, et al. Adsorption of creatinine on active carbons with acid hydrothermal modification. Journal of the Taiwan institute of Chemical Engineers, 66 (2016): 347-356.

[11] Z. Izakmehri, M. Darvish Ganji, M. Ardjmand. Adsorption of 2, 3, 7, 8-tetrachlorodibenzo-p-dioxin (TCDD) on pristine, defected and Al-doped carbon nanotube: A dispersion corrected DFT study. Vacuum, 136 (2017): 51-59.

[12] G.T. Li, Y.M. Feng, X.Q. Chai, et al. Adsorption of cyclic organics generated during electrochemical oxidation of Orange II by activated carbon fibers and toxicity test. Journal of Water Process Engineering, 7 (2015): 21-26.

[13] J.L. Li, A.F. He, J. Jiang, et al. Quantitative relationship between the adsorptivity of carbonaceous materials in soil for Pb (II) and soil organic matter content. Science of the Total Enviroment, 572 (2016): 369-378.

[14] M.Ahamad, A.U. Rajapaksha, J.E. Lim, et al. Biochar as a sorbent for contaminant management in soil and water: A review. Chemosphere, 99 (2014): 19-23.

[15] M.K. Hossain, V. Sterzov, K.Y. Chan et al. Influence of pyrolysis temperature on production and nutrient properties of wastewater sludge biochar. J. Environ. Manage., 92 (2014): 223-228.

[16] D. C. Guo, J. Mi, G. P. Hao, et al. Ionic liquid C16minBF$_4$ assisted synthesis of poly (benzoxazine-co-resol)-based hierarchically porous carbons with superior performance in supercapacitors. Energy & Environmental Science, 6 (2013): 652-659.

[17] T. Tooming, T. Thomberg, H. Kuring, et al. High powder density supercapacitors based on the carbon dioxide activated d-glucose derived carbon electrodes and 1-ethyl-3-methlimidazolium tetrafluoroborate ionic liquid. Journal of Powder Source, 280 (2015): 667-677.

[18] M. Plaza-Recobert, G. Trautwein, M. Pérez-Cadenas, et al. Preparation of binderless activated carbon monoliths from cocoa bean husk. Microporous and

Mesoporous Materials, 243 (2017): 28-38.

[19] G. Nam, J. Park, S.T. Kim, et al. Metal-Free Ketjenblack Incoporated Nitrogen-Doped Carbon Sheets Derived from Gelatin as Oxygen Reduction Catalysts. Nano Letters, 14 (2014): 1870-1876.

[20] J. Zhou, Z.P Qiu, J.K. Zhou, et al. Hierarchical porous carbons from alkaline poplar bark extractive-based phenolic resin for supercapacitors. Electrochimica Acta, 180 (2015): 1007-1013.

[21] F. Beshkar, H. Khojasteh, M. Salavati-Niasari. Recyclable magnetic superhydrophobic straw soot sponge for highly efficient oil/water separation. Journal of Colloid and Interface Science, 497 (2017): 57-65.

[22] M. Samouhos, M. Taxiarchous, G. Piatos, et al. Controlled reduction of red mud by H_2 followed by magnetic separation. Minerals Engineering, 105 (2017): 36-43.

[23] Z.H. Xiao, R. Zhang, X.Y. Chen, et al. Magnetically recoverable Ni@carbon nanocomposites: Solid-state synthesis and the application as excellent adsorbents for heavy metal ions. Applied Surface Science, 263 (2012): 795-803.

[24] Y.H. Ni, L. Jin, L. Zhang, et al. Honeycomb-like Ni@C composites nanostructures: synthesis, properties and applications in the dectection of glucose and the removal of heavy-metal ions. J. Matter. Chem. 20 (2010): 6430-6436.

[25] L. Ning, X.G. Li, Y.L. Sun, et al. Synthesis and characteristic of carbon encapsulated ferronickel nanoparticles by detonation decomposition of doping with nitrate explosive precursors. J. Alloys Compd. 505 (2010): 352-356.

[26] C. Yu, J.S. Qiu. Preparation and magnetic behavior of carbon-encapsulated cobalt

and nickel nanoparticles from starch. Chem. Eng. Res. Des. 86 (2008): 904-908.

[27] X. Yu, X. Cui, A. Gangnoud, et al. Macroscopic cross-linked Ni@C composite with high porosity by a novel salt-templating process. Journal of Alloys and Compounds, 687 (2016): 867-874.

[28] S.C. Xu, N.L. Zhang, J.F. Yang, et al. Silicon carbide-based foams derived from foamed SiC-filled phenolic resin by reactive infiltration of silicon. Ceramics International, 42 (2016): 14760-14764.

[29] Z.H. Wang, C.Z Wang, J.J. Yuan, et al. Adsorption characteristics of adsorbent resins and antioxidant capacity for enrichment of phenolics from two-phase olive waste. Journal of Chromatography B, 1040 (2017): 38-46.

[30] G.C. Lv, Z.H. L, W.T. Jiang, et al. Removal of Cr(VI) from water using Fe(II)-modified natural zeolite. Chemical Engineering Research & Design, 92 (2014): 384-390.

[31] Z.H. Liu, Analytical Chemical Handbook. Beijing: Chemical industry press, 1998.

[32] Z.C. Bai, Z.C. Ju, C.L. Guo, et al. Direct large-scale synthesis of 3D hierarchical mesporous NiO microspheres as high-performance anode materials for lithium ion batteries. Nanoscale, 6 (2014): 3286-3273.

[33] Y.X. Song, T.T. Qiang, M. Ye, et al. Metal organic framework derived magnetically separable 3-dimensional hierarchical Ni@C nanocomposites: Synthesis and adsorption properties. Applied Surface Science, 359 (2015): 834-840.

[34] Z.H. Sun, L.F. Wang, P.P. Liu, et al. Magnetically Motive Porous Sphere Composites and its Excellent Properties for the Removal of Pollutants in Water by Adsorption and Desorption Cycles. Adv. Matter. 18 (2006): 1968-1973.

[35] J.H. Wang, L.J. Bi, Y.F. Ji, et al. Interaction between lysozyme and humic acid in layer-by –layer assemblies: Effects of pH and ionic strength. J. Colloid Interface Sci. 430 (2014): 140-146.

[36] I.P. Pozdnyakov, V.F. Plyusnin, V.P. Grivin, Photochemistry of Fe(III) and sulfosalicylic acid aqueous solutions. J. Photoch. Photobio. A 182(2012)75-81.

[37] Z.H. Li, P.H. Chang, J.S. Jean, Mechanism of chlorpheniramine adsorption on Ca-montmorillonite, Colloid Surface A 385 (2011)213-218.

[38] N A. Ücer, A. Uyanik, S.F. Aygün, Adsorption of Cu, Cd, Zn, Mn and Fe ions by tannic acid immobilised activated carbon, Separation and Purification Technology, 47 (2006) 113-118.

[39] N A. Ücer, A. Uyanik, S. Cay, Y. Özkan, Immobilisation of tannic acid onto activated carbon to improve Fe(Ⅲ) adsorption, Separation and Purification Technology, 44 (2005) 11-17.

[40] H.P. Zhang, L.Q. Gu, L. Zhang, et al. Removal of aqueous Pb(II) by adsorption on Al_2O_3-pillared layered MnO_2. Applied Surface Science, 406 (2017): 330-338.

[41] Z.L. Cheng, Y.X. Li, Z. L. Novel adsorption materials based on graphene oxide/Beta zeolite composite materials and their adsorption performance for rhodamine B. Journal of Alloys and Compounds, 708 (2017): 255-263.

[42] N. Chiron, R. Guiler, E. Deydier. Adsorption of Cu (Ⅱ) and Pb (Ⅱ) onto a grafted

silica: isotherms and kinetic models. Water Res. 37 (2003): 3079-2086.

[43] D. Qin, X. Niu, M. Qiao, Adsorption of ferrous ions onto montmorillonites, Appl. Surf. Sci. 333(2015)170-177.

[44] I. Langmuir. The adsorption of gases on plane surfaces of glass, mica, and platinum. J. Am. Chem. Soc, 40 (1918): 1361-1403.

[45] C. Xia, G.C. Lv, L.F. Mei, Removal of Chlorpheniramine from Water by Birnessite, Water Air Soil Poll. 225(2014)2130-2139.

[46] S.P. Chen, J.X. Hong, H.X. Yang, Adsoption of uranium (Ⅵ) from aqueous solution using a novel graphene oxide-actived carbon felt composite, J. Environ. Radioactiv. 126(2013)253-258.